ChemComm

COMMUNICATION

View Article Online
View Journal | View Issue

Cite this: *Chem. Commun.*, 2021, **57**, 13772

Received 23rd September 2021,
Accepted 30th November 2021

DOI: 10.1039/d1cc05377a

rsc.li/chemcomm

Ethylene oligomerization on Ni^{2+} single sites within lacunary defects of Wells Dawson polyoxometalates†

Yoonrae Cho, [a] Jessica A. Muhlenkamp,[a] Allen G. Oliver[b] and Jason C. Hicks *[a]

Oligomerization of light olefins has become an essential step to convert gaseous olefins to liquid fuels and value-added chemicals. Here, we report the synthesis and application of nickel single sites isolated on Wells Dawson polyoxometalate defects as stable and regenerable catalysts for ethylene oligomerization.

The emerging production of shale gas liquids has resulted in the need for more sustainable utilization of these resources, specifically for olefin production.[1] Oligomerization is an essential catalytic step to convert light olefins into heavier liquid fuels or value-added chemicals such as linear alpha olefins.[2–4] Homogeneous catalytic olefin oligomerization processes (*e.g.*, Shell Higher Olefin Process) use soluble nickel complexes activated by pyrophoric methyl-aluminoxane (MAO) based co-catalysts and require complex separation processes to recycle the catalyst.[4,5] To avoid the intrinsic drawbacks of homogeneous processes, Ni-containing metal organic frameworks (MOFs), nickel sulfate impregnated on various metal oxides, and Ni^{2+} cations exchanged on both non-porous inorganic clays and porous entities such as zeolites and mesoporous aluminosilicates have been synthesized and used as platforms for isolating Ni for olefin oligomerization.[3,4,6–18] Despite the ability to isolate Ni-based single sites in MOFs, they often require activation by MAO similar to homogeneous Ni(II) catalysts, and the reactivity of these catalysts is reported to decrease when operated above room temperature.[11–13] Additionally, the turnover frequency of Ni containing MOFs substantially decreases under flow conditions without the addition of MAO as a co-catalyst.[13] Ni^{2+} cations exchanged on proximal Brønsted acid sites in zeolites are possibly the most widely investigated solid catalysts for ethylene oligomerization owing to the well-defined and robust microporous framework.[3,4,6–10,14] However, these materials deactivate likely due to nickel mobility in the presence of light olefins and the subsequent formation of bridging metal–olefin–metal complexes.[19,20]

Lyon *et al.* first reported the synthesis of transition metal monosubstituted Wells Dawson phosphotungstate polyoxometalate (POM),[21] and Song and co-workers developed the synthetic strategy to substitute different transition metal ions into lacunary defects to tune the redox properties of POMs.[22,23] Under mildly basic conditions (pH of 7 to 8), a tungsten and oxygen atom from capping tungsten oxides are eliminated from the Wells Dawson phosphotungstate structure. This base degradation creates a lacunary defect (negatively charged (−4) vacancy) which is capable of bearing a metal ion. Recently, Gao *et al.* reported the chelation of histidine molecules with isolated transition metal atoms (Ni, Co, Cu, Fe and Mn) substituted on the lacunary defects of Wells Dawson phosphotungstate.[21,24] We hypothesized similarly that isolated nickel ions formed on the lacunary defects of the Wells Dawson structure could serve as potentially stable, single sites capable of facilitating ethylene oligomerization. We report here the preparation and performance evaluation of Ni^{2+} active sites incorporated in the lacunary defects of Wells Dawson phosphotungstate for the conversion of ethylene into heavier oligomeric products without a cocatalyst. Furthermore, the kinetic parameters of Ni^{2+} sites were also established and compared to literature reports. Lastly, the nickel substituted POM catalyst was regenerated by removal of heavy oligomeric surface species *via* thermal treatment in an inert environment.

The Wells Dawson $K_6P_2W_{18}O_{62}$ (α/β-POM-WD) and lacunary structure, $K_{10}P_2W_{17}O_{61}$ (α_2-Lacunary POM-WD) were synthesized by following literature reports (see ESI,† Fig. S1).[21,25] The lacunary vacant sites were subsequently metallated with $Ni(NO_3)_2$ *via* a stoichiometric aqueous phase ion-exchange process to form Ni-POM-WD.[21] The anionic structure of Ni-POM-WD was confirmed *via* single crystal X-ray crystallography, which matched the desired Wells Dawson structure bearing the nickel site on one of the three capping tungsten oxides

[a] *Department of Chemical and Biomolecular Engineering, University of Notre Dame, 250 Nieuwland Hall, Notre Dame, IN 46556. E-mail: jhicks3@nd.edu*
[b] *Department of Chemistry and Biochemistry, University of Notre Dame, 251 Nieuwland Hall, Notre Dame, IN 46556*

† Electronic supplementary information (ESI) available. See DOI: 10.1039/d1cc05377a

(Fig. S2, ESI†). The phosphorous features of α-POM-WD, α_2-lacunary POM-WD and Ni-POM-WD were analysed by solution phase ^{31}P NMR in 90/10 H_2O/D_2O. As shown in Fig. S3 (ESI†), one phosphorous feature from α-POM-WD appears at −13.1 ppm after the purification from its mixture with β-POM-WD, which shows two peaks at −11.6 and −12.4 ppm (Fig. S3a and b, ESI†). Once the vacant defect is formed from α-POM-WD, a new P peak at −7.5 ppm is observed due to the different surrounding environment of the internal phosphate close to the defect (Fig. S3c, ESI†). This peak at −7.5 ppm in α_2-lacunary POM-WD drastically shifts and appears as a broad peak at 200–250 ppm (Fig. S4, ESI†) in Ni-POM-WD. This shift was caused by the introduction of the paramagnetic Ni^{2+} cation and suggests that lacunary sites are successfully substituted with Ni. The molecular bonding features were evaluated *via* FTIR (Fig. S5, ESI†). The P–O vibration of internal phosphates and the splitting of this feature upon the lacunary formation were observed at 1086 cm^{-1}. Additionally, terminal W=O_d at 957 cm^{-1}, inter bridging W–O–W stretching features at 908 cm^{-1} and intra bridging W–O–W features at 730–780 cm^{-1} were also present.[21,22] The Ni2p3/2 X-ray photoelectron spectroscopy (XPS) analysis of the Ni-POM-WD shows a binding energy of $Ni2p_{3/2}$ at 856.8 eV which is attributed to the pseudo tetrahedral cationic Ni^{2+} sites and resembles that of Ni^{2+} exchanged aluminosilicates (Fig. S6, ESI†).[26,27]

The synthesized Ni-POM-WD structures were loaded onto an SBA-15 support using incipient wetness impregnation (Fig. 1a). The textural properties of SBA-15 and Ni-POM-WD/SBA-15 along with the nickel loadings of these materials are presented in Table S1 (ESI†). After supporting Ni-POM-WD on SBA-15, the Ni-POM-WD structure was retained, as evidenced by solid state MAS ^{31}P NMR which shows the presence of a matching peak at −21.6 ppm with unsupported Ni-POM-WD (Fig. 1b). High-angle annular dark-field scanning transmission electron microscopy (HAADF-STEM) images and energy dispersive X-ray (EDX) Ni elemental mapping of Ni-POM-WD/SBA-15 are provided in Fig. 1c. The supported Ni-POM-WD is observed within the mesoporous domains, and the Ni is dispersed across the SBA-15 particle. Ethylene oligomerization experiments were conducted in a flow reactor with a pure ethylene feed at 200 °C and 2 MPa (Fig. 1d). As shown in Fig. 1d, control experiments of both of SBA-15 alone and non-metallated α-POM-WD supported on SBA-15 were relatively inactive for the oligomerization reaction. Interestingly, unsupported Ni-POM-WD crystals were also inactive under the same condition. This result is potentially due to the inaccessibility of Ni sites in the bulk Ni-POM-WD crystals. Once the Ni-POM-WD was dispersed on SBA-15, an ethylene consumption rate of 152 mmol g_{cat}^{-1} h^{-1} at 45 minutes time on stream (TOS) was observed. The observed deactivation trajectory follows that of previously reported cationic Ni^{2+} active sites in zeolites used for ethylene oligomerization.[9,18–20,28,29]

Additional experiments were conducted to obtain the experimental rate order and activation barrier for the Ni-POM-WD/SBA-15 catalyst. The rate order was obtained from a set of ethylene pressure sweep experiments (Fig. 2a). The initial dimerization rates were obtained under a 30 mL min^{-1} pure ethylene flow at 200 °C and pressures ranging from 0.62 to 2.0 MPa (Fig. S7, ESI†). The apparent reaction order of the

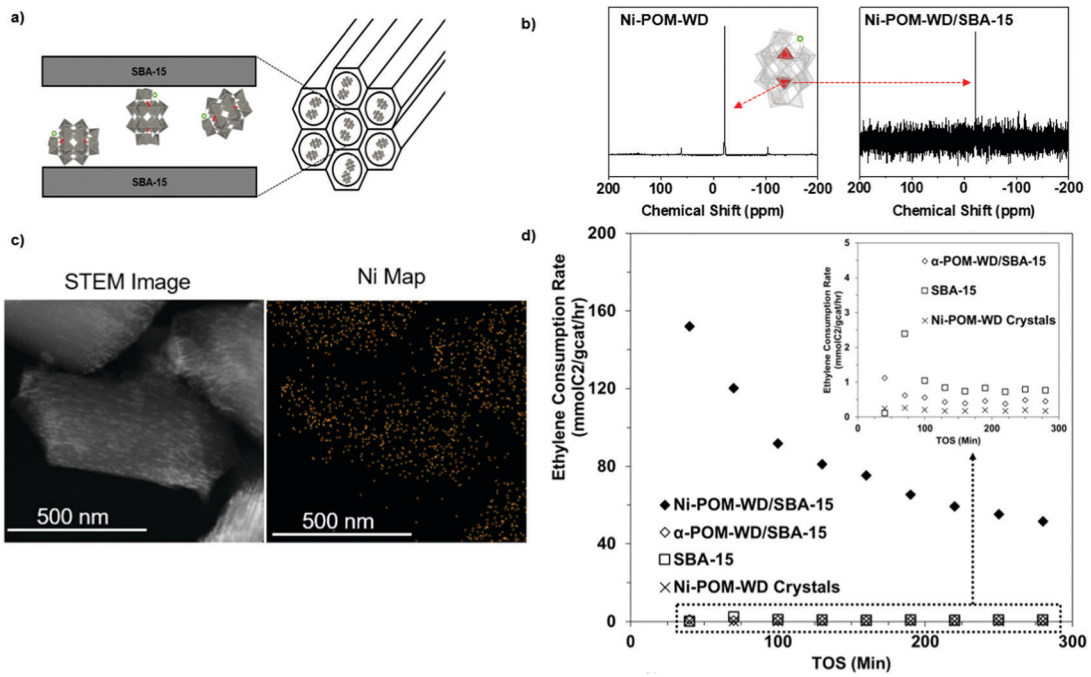

Fig. 1 (a) Cartoon representation of Ni-POM-WD in mesopores of SBA-15, (b) solid state MAS ^{31}P NMR of unsupported Ni-POM-WD (left) and Ni-POM-WD/SBA-15 (right), (c) HAADF-STEM image and EDX Ni mapping of fresh Ni-POM-WD/SBA-15, (d) ethylene consumption rate of Ni-POM-WD/SBA-15 and control materials under pure ethylene flow at 200 °C at 2 MPa (inset provides a closer view of the background reactivity of the control materials).

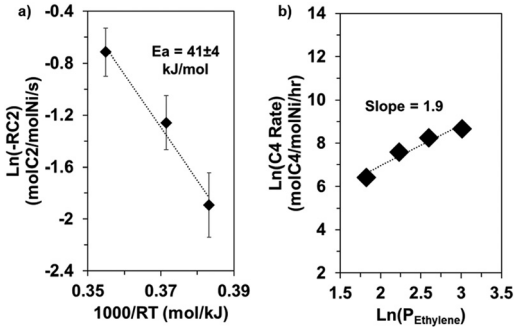

Fig. 2 (a) Ethylene pressure sweep for the reaction order calculation of butene production, (b) Arrhenius plot for activation energy determination.

initial dimerization was calculated as 1.9, which is similar to the rate order reported on Ni^{2+} exchanged SSZ-24 (2.0) and MCM-41 (2).[6,30] The observed second order dependence on ethylene pressure suggests that an ethylene surface species bound to an Ni^{2+} site undergoes dimerization with gaseous ethylene as previously reported.[6,30] The reported dimerization event between gaseous and surface ethylene species was further probed by performing partial pressure sweep experiments with a diluted feed stream at each of the end points (0.62 and 2.0 MPa) shown in Fig. 2a. In the regime where the ethylene partial pressure is low, the ethylene pressure dependence was observed as second order (Fig. S8 and Scheme S1, ESI†). In the relatively high ethylene partial pressure regime, the ethylene pressure term in the denominator dominates and results in the observance of first order dependence (Fig. S8 and Scheme S1, ESI†). As shown in Fig. 2b, the apparent activation energy was determined from the averaged ethylene consumption rates (Fig. S9, ESI†) to be 41 kJ mol^{-1}, which again resembles the reported activation barriers for ethylene oligomerization on Ni^{2+} exchanged zeolites in literature (33 to 45 kJ mol^{-1}) and also resides within the reported range of activation energy values (10 to 88 kJ mol^{-1}) of other Ni based mesoporous aluminosilicates.[6,8,10,31]

Fig. 3 provides the ratio of 1-butene to 2-butene and the selectivity among C4 isomers as a function of the ethylene conversion. The product distribution at similar ethylene conversions was analysed and compared to the reported literature on Ni^{2+} exchanged SSZ-24.[6] As expected, all three of the observed dimeric products were linear butenes. Isobutene, which is known to be the product of skeletal isomerization occurring on residual Brønsted acid sites, was not observed in the product stream.[6] The absence of isobutene further indicates that the Ni sites on Wells Dawson defects are the primary active site contributing to the ethylene oligomerization. In addition to the absence of isobutene, pyridine diffuse reflectance infrared Fourier transform spectroscopy (DRIFTS) experiments were conducted with Ni-POM-WD. Peaks associated with pyridinium ions formed during the protonation of pyridine by Brønsted acid sites (1639 cm^{-1} and 1544 cm^{-1}) were not observed (Fig. S10, ESI†).[9,32] As the ethylene conversion increases, more *cis*- and *trans*-2-butenes were observed as shown in Fig. 3. These internal butene species are reported to be a product of parallel isomerization which involves 1-butene adsorbing on the Ni^{2+} sites and forming two isomers of internal linear butenes as a part of the Cossee-Arlman mechanism.[6,9,33,34] Together, the kinetic parameters and the product distribution of Ni-POM-WD indicate that the substituted Ni sites resemble the ethylene oligomerization occurring on Ni^{2+} exchanged zeolites.

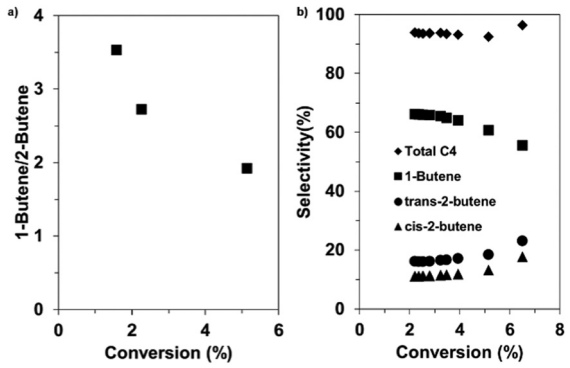

Fig. 3 (a) 1-Butene/2-butene, (b) product selectivity *vs.* conversion at 200 °C at 2 MPa.

The Ni-POM-WD/SBA-15 was characterized in detail after reaction *via* HAADF-STEM and solid-state MAS ^{31}P NMR. Fig. S11 (ESI†) provides HAADF STEM images of Ni-POM/SBA-15 before (a) and after (b) ethylene oligomerization. Agglomeration of the dispersed Ni-POM-WD structures was not observed for either sample from the STEM images or the elemental EDX mappings. In both the fresh and used catalysts, there was also no sign of Ni nanoparticle formation in the EDX mapping. The fresh Ni-POM-WSD/SBA-15 sample displayed a chemical shift at −21.6 ppm from its solid-state MAS ^{31}P NMR, and the used catalyst bed showed the same peak at −21.6 ppm (Fig. S12, ESI†), demonstrating the Ni-POM-WD structure was preserved after reaction at 200 °C and 2 MPa. Visual inspection and thermogravimetric profiles of fresh and spent Ni-POM-WD/SBA-15 showed no sign of coke formation. The thermogravimetric analysis showed the expected loss of hydration water starting at 221 °C (Fig. S13, ESI†).

The regenerability of the Ni-POM-WD catalysts after reaction at 200 °C and 2 MPa was subsequently investigated. In order to regenerate the catalysts, desorbed products and remaining reactants were purged with helium at 200 °C. The temperature was then raised to 300 °C to evaporate and desorb heavy products under a constant flow of helium. The helium thermal treatment was conducted for 12 hours, at which point the temperature was adjusted back to 200 °C. The ethylene feed stream was then re-introduced. The results from the regeneration studies are shown in Fig. 4. As a result of this regeneration process, the initial maximum ethylene conversion (evaluated at 35 min TOS) of 26.4% was almost completely recovered with 25.7% and 25.1% conversions observed after the first and second recycle, respectively (Fig. S14 and S15, ESI†). The C4 and C6+ selectivity during the runs after the first and second recycles were also similar to the fresh catalysts. These results imply that the intrinsic nature of nickel sites on the lacunary defects are preserved during regeneration, and the initial catalytic

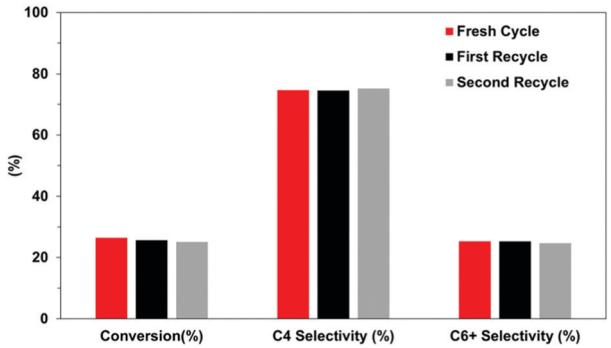

Fig. 4 Regenerated ethylene oligomerization *via* thermal helium treatment.

performance is successfully recovered by simple removal of heavy oligomeric products.

In conclusion, Ni can be effectively incorporated into the defects of Wells Dawson polyoxometalate and used to catalyse the oligomerization of ethylene when supported on SBA-15. The Ni speciation of the metallated defect site resembles that of Ni^{2+} exchanged zeolites. The stability of Ni-POM-WD is maintained during the ethylene oligomerization at 200 °C and 2 MPa. We also demonstrated that Ni-POM-WD can be effectively regenerated for ethylene oligomerization through a simple heat treatment in helium. Although Ni migration and pairing has been proposed as a source of deactivation in Ni^{2+} exchanged zeolites, there was no indication of site leaching and migration of the leached Ni species with Ni-POM-WD. Another potential source of catalyst deactivation is heavy oligomeric products blocking active sites and preventing light olefin adsorption.[3,19] Because the Ni-POM-WD catalyst structures remained intact after the reaction and the thermal helium treatment was sufficient to recover initial maximum reactivity, it is hypothesized that the observed time-on-stream deactivation occurs through site blockage by heavier oligomers. Overall, polyoxometalates were shown to be a versatile, well-defined platform to isolate Ni^{2+} single sites for olefin oligomerization reactions with immense opportunity for study in other catalytic applications.

This work was supported in part by the Engineering Research Centers Program of the National Science Foundation under NSF Cooperative Agreement no. EEC-1647722. The authors would like to thank the Defense University Research Instrumentation Program under AFOSR Award no. FA9550-17-1-0376. The authors would also like to thank the Notre Dame Integrated Imaging Facility, the Center for Environmental Science and Technology, and the Notre Dame Molecular Structure Facility for use of their facilities.

Conflicts of interest

There are no conflicts to declare.

Notes and references

1 E. E. Stangland, *Annu. Rev. Chem. Biomol. Eng.*, 2018, **9**, 341–364.
2 J. J. Siirola, *AIChE J.*, 2014, **60**, 810–819.
3 R. Joshi, A. Saxena and R. Gounder, *Catal. Sci. Technol.*, 2020, **10**, 7101–7123.
4 A. Finiels, F. Fajula and V. Hulea, *Catal. Sci. Technol.*, 2014, **4**, 2412–2426.
5 W. Keim, *Angew. Chem., Int. Ed.*, 2013, **52**, 12492–12496.
6 R. Y. Brogaard, M. Kømurcu, M. M. Dyballa, A. Botan, V. van Speybroeck, U. Olsbye and K. de Wispelaere, *ACS Catal.*, 2019, **9**, 5645–5650.
7 R. Y. Brogaard and U. Olsbye, *ACS Catal.*, 2016, **6**, 1205–1214.
8 L. Riekert, *J. Catal.*, 1970, **19**, 8–14.
9 R. Joshi, G. Zhang, J. T. Miller and R. Gounder, *ACS Catal.*, 2018, **8**, 11407–11422.
10 G. V. S. Seufitelli, J. J. W. Park, P. N. Tran, A. Dichiara, F. L. P. Resende and R. Gustafson, *J. Catal.*, 2021, **401**, 40–53.
11 J. Canivet, S. Aguado, Y. Schuurman and D. Farrusseng, *J. Am. Chem. Soc.*, 2013, **135**, 4195–4198.
12 E. D. Metzger, R. J. Comito, Z. Wu, G. Zhang, R. C. Dubey, W. Xu, J. T. Miller and M. Dincă, *ACS Sustainable Chem. Eng.*, 2019, **7**, 6654–6661.
13 Z. Li, N. M. Schweitzer, A. B. League, V. Bernales, A. W. Peters, A. "Bean" Getsoian, T. C. Wang, J. T. Miller, A. Vjunov, J. L. Fulton, J. A. Lercher, C. J. Cramer, L. Gagliardi, J. T. Hupp and O. K. Farha, *J. Am. Chem. Soc.*, 2016, **138**, 1977–1982.
14 S. Moussa, P. Concepción, M. A. Arribas and A. Martínez, *ACS Catal.*, 2018, **8**, 3903–3912.
15 V. Hulea, *ACS Catal.*, 2018, **8**, 3263–3279.
16 R. Beucher, V. Hulea and C. Cammarano, *React. Chem. Eng.*, 2022, DOI: 10.1039/D1RE00258A.
17 A. Aid, R. D. Andrei, S. Amokrane, C. Cammarano, D. Nibou and V. Hulea, *Appl. Clay Sci.*, 2017, **146**, 432–438.
18 R. D. Andrei, E. Borodina, D. Minoux, N. Nesterenko, J.-P. Dath, C. Cammarano and V. Hulea, *Ind. Eng. Chem. Res.*, 2020, **59**, 1746–1752.
19 A. N. Mlinar, S. Shylesh, O. C. Ho and A. T. Bell, *ACS Catal.*, 2014, **4**, 337–343.
20 A. N. Mlinar, G. B. Baur, G. G. Bong, A. "Bean" Getsoian and A. T. Bell, *J. Catal.*, 2012, **296**, 156–164.
21 D. K. Lyon, W. K. Miller, T. Novet, P. J. Domaille, E. Evitt, D. C. Johnson and R. G. Finke, *J. Am. Chem. Soc.*, 1991, **113**, 7209–7221.
22 J. H. Choi, J. K. Kim, S. Park, J. H. Song and I. K. Song, *Appl. Catal., A*, 2012, **427–428**, 79–84.
23 J. H. Choi, J. K. Kim, D. R. Park, T. H. Kang, J. H. Song and I. K. Song, *J. Mol. Catal. A: Chem.*, 2013, **371**, 111–117.
24 N. Gao, H. Sun, K. Dong, J. Ren, T. Duan, C. Xu and X. Qu, *Nat. Commun.*, 2014, **5**, 3422.
25 B. J. Hornstein and R. G. Finke, *Inorg. Chem.*, 2002, **41**, 2720–2730.
26 R. Baran, I. I. Kamińska, A. Śrębowata and S. Dzwigaj, *Microporous Mesoporous Mater.*, 2013, **169**, 120–127.
27 S. Kirumakki, B. Shpeizer, G. Sagar, K. Chary and A. Clearfield, *J. Catal.*, 2006, **242**, 319–331.
28 O. Jan, K. Song, A. Dichiara and F. L. P. Resende, *Ind. Eng. Chem. Res.*, 2018, **57**, 10241–10250.
29 A. Ehrmaier, Y. Liu, S. Peitz, A. Jentys, Y.-H. C. Chin, M. Sanchez-Sanchez, R. Bermejo-Deval and J. Lercher, *ACS Catal.*, 2019, **9**, 315–324.
30 I. Agirrezabal-Telleria and E. Iglesia, *J. Catal.*, 2017, **352**, 505–514.
31 R. L. Espinoza, C. J. Korf, C. P. Nicolaides and R. Snel, *Appl. Catal.*, 1987, **29**, 175–184.
32 I. K. Song and M. A. Barteau, *Korean J. Chem. Eng.*, 2002, **19**, 567–573.
33 F. T. T. Ng and D. C. Creaser, in *Studies in Surface Science and Catalysis*, eds. K. J. Smith and E. C. Sanford, Elsevier, 1992, 73, 123–131.
34 E. D. Metzger, C. K. Brozek, R. J. Comito and M. Dincă, *ACS Cent. Sci.*, 2016, **2**, 148–153.